Anatomy and Decadal Evolution of the Pacific Subtropical–Tropical Cells (STCs)*

ANTONIETTA CAPOTONDI AND MICHAEL A. ALEXANDER

NOAA–CIRES Climate Diagnostics Center, Boulder, Colorado

CLARA DESER

National Center for Atmospheric Research, Boulder, Colorado

MICHAEL J. MCPHADEN

NOAA/Pacific Marine Environmental Laboratory, Seattle, Washington

(Manuscript received 9 September 2004, in final form 25 February 2005)

ABSTRACT

The output from an ocean general circulation model driven by observed surface forcing (1958–97) is used to examine the evolution and relative timing of the different branches of the Pacific Subtropical–Tropical Cells (STCs) at both interannual and decadal time scales, with emphasis on the 1976–77 climate shift. The STCs consist of equatorward pycnocline transports in the ocean interior and in the western boundary current, equatorial upwelling, and poleward flow in the surface Ekman layer. The interior pycnocline transports exhibit a decreasing trend after the mid-1970s, in agreement with observational transport estimates, and are largely anticorrelated with both the Ekman transports and the boundary current transports at the same latitudes. The boundary current changes tend to compensate for the interior changes at both interannual and decadal time scales. The meridional transport convergence across 9°S and 9°N as well as the equatorial upwelling are strongly correlated with the changes in sea surface temperature (SST) in the central and eastern equatorial Pacific. However, meridional transport variations do not occur simultaneously at each longitude, so that to understand the phase relationship between transport and SST variations it is important to consider the baroclinic ocean adjustment through westward-propagating Rossby waves. The anticorrelation between boundary current changes and interior transport changes can also be understood in terms of the baroclinic adjustment process. In this simulation, the pycnocline transport variations appear to be primarily confined within the Tropics, with maxima around 10°S and 13°N, and related to the local wind forcing; a somewhat different perspective from previous studies that have emphasized the role of wind variations in the subtropics.

1. Introduction

Several recent studies have found evidence for climate variability on decadal time scales in both the tropical and extratropical Pacific (e.g., Trenberth 1990; Tanimoto et al. 1993; Wang and Ropelewski 1995; Mantua et al. 1997; Zhang et al. 1997; Deser et al. 2004). A well-known example is the "shift" in the atmosphere–ocean system that took place in 1976–77 (Nitta and Yamada 1989; Trenberth and Hurrell 1994; Yasuda and Hanawa 1997). Because of the longer time scales involved in the oceanic adjustment compared to the atmosphere, oceanic processes are likely involved in the origin of decadal time scales of climate variability. Several mechanisms have been proposed to explain decadal variability in the Tropics and extratropics. Some mechanisms invoke air–sea interactions and adjustment of the ocean circulation through Rossby wave propagation in midlatitudes (Latif and Barnett 1996); others are based on tropical–subtropical interactions (Gu and Philander 1997; Kleeman et al. 1999; Solomon et al. 2003) or rely on processes within the tropical band (Knudson and Manabe 1998; Chang et al. 2001; Luo and Yamagata 2001; Timmermann and Jin 2002).

* Pacific Marine Environmental Laboratory Publication Number 2734.

Corresponding author address: Dr. Antonietta Capotondi, NOAA–CIRES Climate Diagnostic Center, R/CDC1, 325 Broadway, Boulder, CO 80305.
E-mail: Antonietta.Capotondi@noaa.gov

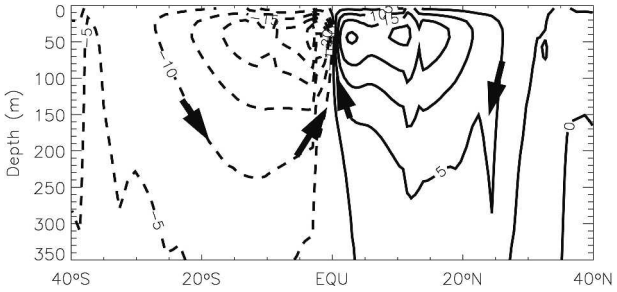

FIG. 1. Meridional streamfunction computed from the NCAR OGCM. Contour interval is 5 Sv. Thick arrows indicate the direction of the zonally averaged circulation.

Two of these mechanisms involve the subtropical–tropical ocean circulation. The wind-driven upper-ocean circulation can be regarded as a shallow overturning cell, the subtropical–tropical cell (STC; McCreary and Lu 1994; Liu 1994), in which subtropical water subducts into the main thermocline, upwells at the equator, and then returns to the subtropics in the thin surface Ekman layer (Fig. 1). The mechanism proposed by Gu and Philander (1997) relies on the subduction of surface temperature anomalies in midlatitudes and their downward and equatorward propagation along mean isopycnals. While observations show evidence of thermal anomalies subducting in the main thermocline in the northern midlatitudes (Deser et al. 1996; Schneider et al. 1999), these anomalies decay away from the subduction region, and the thermocline variability found equatorward of ~18° appears to be primarily associated with tropical wind forcing (Schneider et al. 1999; Capotondi et al. 2003). Thus, it seems unlikely that the Gu and Philander (1997) mechanism can significantly contribute to the modulation of equatorial SST anomalies on decadal time scales.

An alternative hypothesis is that changes in the winds may spin up or slow down the STCs in both the Northern and Southern Hemispheres, thus changing the rate at which water of constant properties is transported toward the equator and consequently altering the strength of equatorial upwelling. This mechanism contrasts with the Gu and Philander (1997) hypothesis, which involves advection of thermal anomalies by the mean circulation. Using an intermediate coupled model, consisting of a 3–1/2 layer shallow water model coupled with a statistical atmosphere, Kleeman et al. (1999) have shown that decadal variations of tropical SSTs can be induced by changes in the subtropical winds. In their ocean model, the strength of the STCs is determined by the meridional transport divergence across 23°N and 23°S, equatorward of which subduction is suppressed. In turn, the meridional transport divergence is set by the Ekman transport divergence along the same latitudes. Thus in their study, changes in equatorial SSTs are primarily related to changes in wind stress and subduction rates in the subtropics (poleward of ~23°).

Subduction rates control the equatorward mass transport in the thermocline. Depending upon the longitude at which water subducts, fluid can reach the equator following a pathway in the ocean interior, or it may reach the western boundary current first and then flow equatorward through the western boundary current pathway (Liu et al. 1994). Thus, the STCs can be viewed as composed of different branches, which include the interior equatorward flow (IN), the equatorward flow in the low-latitude western boundary currents (BCs; consisting of the Mindanao current in the Northern Hemisphere and the New Guinea Coastal Current in the Southern Hemisphere), plus the equatorial upwelling branch (UPW), and the poleward Ekman transport in the surface Ekman layer (EKM). Changes in the winds do not only alter the Ekman divergence and the rate of subduction in the subtropics, but they also change the rate of equatorial upwelling.

To better understand how subtropical wind stress variations can influence equatorial SSTs, Klinger et al. (2002) forced the ocean component of the coupled model used by Kleeman et al. (1999) with idealized wind fields and examined the evolution of the different branches of the model STC (with the exclusion of the western boundary transport) from a zonally averaged perspective. Their conclusions are that the interior thermocline transport is weaker than the Ekman transport and equatorial upwelling. Moreover, the interior transport lags the equatorial SST variations, a result that appears in disagreement with the hypothesized causal relationships between thermocline transport and SST variations. In Klinger et al.'s (2002) study, equatorial SSTs are almost coincident with, but slightly lag, changes in surface Ekman transport and equatorial upwelling, so that the surface and upwelling branches appear to be better predictors of the influence of subtropical winds upon equatorial SSTs. Thus, the study of Klinger et al. (2002) raises some questions about the interplay and relative timing of the different STC's branches, and their role in equatorial SST variations.

Using an ocean general circulation model (OGCM) forced by observed winds, Nonaka et al. (2002) find that equatorial winds (5°S–5°N) are as important as extraequatorial winds (poleward of 5°) for the decadal modulation of equatorial SSTs. The processes by which extraequatorial winds affect equatorial SSTs involve the spinup and spindown of the STCs, as described by

Kleeman et al. (1999) and Klinger et al. (2002). Nonaka et al. (2002) also note that wind stress variations poleward of 20°S and 25°N do not seem to play any significant role in forcing equatorial SST anomalies.

The mechanism of tropical decadal variability proposed by Kleeman et al. (1999) is supported by the observational study of McPhaden and Zhang (2002, hereafter MPZ). Using subsurface measurements, MPZ have shown that the increase in equatorial SSTs over the last 50 yr is associated with decreased zonally averaged equatorward transports at 9°S and 9°N in the ocean interior. Because of the sparsity of subsurface observations, the data were binned over time intervals of approximately 10 yr, yielding four transport estimates over a 50-yr period. Thus, the phase relationship between interior mass convergence and SST variations could not be easily established. Since the available observations are unable to resolve the western boundary currents, the western boundary current transports were computed as differences between the surface Ekman transports and the interior transports. However, different wind products can produce very different estimates of Ekman transports, introducing large uncertainties in the estimates of both Ekman and boundary current transports. MPZ also found that decadal changes in boundary current transports could not be detected above the noise level of their calculation. Estimates of the Mindanao Current transport inferred from tide gauge data (Lukas 1988) showed, on the other hand, transport variations concurrent with El Niño–Southern Oscillation (ENSO) events, and the modeling study of Springer et al. (1990) showed anticorrelated boundary and interior transports around 5°N (S) over the period 1979–83. Using a model simulation for the period 1980–2000, Lee and Fukumori (2003, hereafter LF03) have shown the tendency for the boundary current transports to compensate the interior transport changes at both interannual and decadal time scales, a result supported by satellite altimetry observations. The variability of the boundary current and interior transports, and the possibility of a partial compensation of the two on decadal time scales, can be very important for the heat budget of the tropical Pacific (Hazeleger et al. 2004). Another open question concerns the influence of the Indonesian Throughflow (ITF) in the mass balance of the tropical Pacific. The Mindanao Current is considered the major source of ITF water. Do transport changes in the Mindanao Current affect the tropical Pacific mass balance, or do they exit the Pacific basin through the ITF?

In this paper, we use an OGCM driven by observed surface forcing to examine the evolution of the different branches of the Pacific STCs across a broad range of time scales from interannual to decadal–interdecadal. The advantages of using a realistic OGCM include not only the availability of complete information in space and time, but also consistency between variations in wind forcing and ocean circulation. The OGCM we are using is global and includes an ITF, so that ITF variations can be explicitly estimated from the model. The specific questions we focus upon are as follows: 1) What is the relative timing and phase relationship of the different branches of the STC? 2) What is the relationship between the STC components and tropical SST changes from both a zonally averaged and three-dimensional perspective? And 3) what is the latitudinal range over which decadal changes in ocean circulation are significant? Do they extend to the subtropics, as described by Kleeman et al. (1999), or are they limited to the tropical region?

We start our analyses by examining the zonally averaged equatorward transports at 9°S and 9°N, using a methodology very similar to the one adopted by MPZ. After comparing the model's transport estimates with the observational estimates, we exploit the completeness of the model data and their consistency with the surface wind forcing, to sharpen the observational perspective; in particular, we will examine the evolution of the transports at a finer time resolution, as well as the relationship between interior transport and boundary and Ekman transports. We then consider the three-dimensional evolution of the STCs and examine the relative contribution of the different STC branches to the SST changes while the system is adjusting. Both interannual and decadal–interdecadal time scales will be examined, but our major focus will be on the decadal–interdecadal variations, and in particular those associated with the 1976–77 climate shift. Thus, our study will extend the modeling study of LF03 (1980–2000) by including the changes that took place across the mid-1970s.

The paper is organized as follows: In section 2 we describe the model used for this study; in section 3 we consider the relationship between the different components of the STCs and equatorial SSTs; in section 4 we examine the three-dimensional evolution of the STCs; and in section 5 we determine the latitudinal range about the equator over which upper-ocean changes associated with decadal variability are significant. Conclusions are given in section 6.

2. The OGCM

The OGCM used for this study is the National Center for Atmospheric Research (NCAR) ocean model (NCOM) that has been described in detail by Large et

al. (1997), Gent et al. (1998), and Large et al. (2001). The specific numerical simulation analyzed here is described in Doney et al. (2003). In this section we only provide a brief summary of the basic model characteristics and information about the surface forcing used for this simulation.

NCOM is derived from the Geophysical Fluid Dynamics Laboratory (GFDL) Modular Ocean Model with the addition of a mesoscale eddy flux parameterization along isopycnal surfaces (Gent and McWilliams 1990) and a nonlocal planetary boundary layer parameterization (Large et al. 1994). The model is global, with a horizontal resolution of 2.4° in longitude and varying resolution in latitude, ranging from 0.6° near the equator to 1.2° at high latitudes. The model version used for this study includes an anisotropic viscosity parameterization (Large et al. 2001) with enhanced viscosity close to ocean boundaries and much weaker viscosity in the ocean interior.

The surface forcing includes momentum, heat, and freshwater fluxes for the period 1958–97. The wind stress is computed from the reanalysis fields produced at the (National Centers for Environmental Prediction) NCEP–NCAR (Kalnay et al. 1996) using bulk formulas. The sensible and latent heat fluxes are computed from the NCEP winds and relative humidity and the model's SSTs using standard air–sea transfer equations (Large and Pond 1982; Large et al. 1997). Sensible and latent heat fluxes depend on the difference between SST and surface air temperature. Since SST and air temperature closely track each other, when observed air temperatures are used in the bulk formulas, as in the present model simulation, the model's SST is relaxed toward observations (Haney 1971). The relaxation time scale is usually short (30–60 days for typical mixed layer depths), so that the SST in the model can be expected to be strongly constrained by the surface forcing rather than by the interior ocean dynamics. In the equatorial region, however, ocean processes (in particular upwelling) have a controlling influence upon SST, and the surface heat fluxes act to damp the SST anomalies. The damping coefficients estimated for the model using a least squares fit approach are negative over most of the tropical Pacific and correspond to damping time scales longer than 30–60 days. For example, the damping time scale in the Niño-3 region, given the average mixed layer depth of ~40 m in that area, is 130 days, a value very close to that estimated from observations (126 ± 3 days) with a similar methodology (Niiler et al. 2004). The NCEP forcing was chosen because of its multidecade history and global coverage. We recognize that the results will be sensitive to the choice of the wind stress forcing, but we expect that our results would not qualitatively change with different forcings.

The numerical simulation is started from an initial condition obtained from a preliminary mean seasonal climatological integration, so that the initial model state is not too different from the mean state characteristic of the 40-yr experiment. To allow for deep ocean adjustment, the model was then run for two identical 40-yr cycles, using the NCEP winds for 1958–97, the second cycle starting from the conditions achieved at the end of the first 40-yr segment. The mismatch between the model state and the forcing at the beginning of the second cycle did not seem to produce any long-term transient behavior. Here we analyze the output for the second 40-yr period using monthly and annual mean values. Some residual drift in temperature and salinity appears to be confined to depths larger than approximately 500 m (Doney et al. 2003).

3. Anatomy of the STCs

a. The pycnocline transport components

From a three-dimensional perspective, the interior transport of the STCs consists of water subducting into the main thermocline along outcrop lines of isopycnals and then flowing equatorward along the mean isopycnals. Since potential vorticity is a quasi-conserved quantity, water parcels approximately follow lines of constant potential vorticity, so that the potential vorticity structure strongly constrains the pathways of the flow. Figure 2 shows the mean potential vorticity on the 25 σ_θ isopycnal, together with the mean velocities in the upper-to-middle pycnocline (the time-averaged velocities integrated from the bottom of the Ekman layer to the depth of the 25 σ_θ isopycnal). The model pycnocline flow is qualitatively consistent with that predicted by the ventilated thermocline theory (Luyten et al. 1983). In the Northern Hemisphere, the presence of the intertropical convergence zone (ITCZ) in the 7°–12°N latitude band is associated with a tongue of high potential vorticity in the eastern side of the basin, which acts as a "barrier" for the flow moving toward the equator. As a consequence, the interior pathways connecting the subtropics to the equator in the Northern Hemisphere are much more convoluted than those in the Southern Hemisphere (Johnson and McPhaden 1999). Comparison with the potential vorticity field computed from observations (Fig. 1b in MPZ) shows that the potential vorticity structure on the 25 σ_θ isopycnal in the model is very similar to the one estimated from observations, although the potential vorticity ridge at 7°–12°N is somewhat weaker in the model than in observations.

Following MPZ, we compute the different compo-

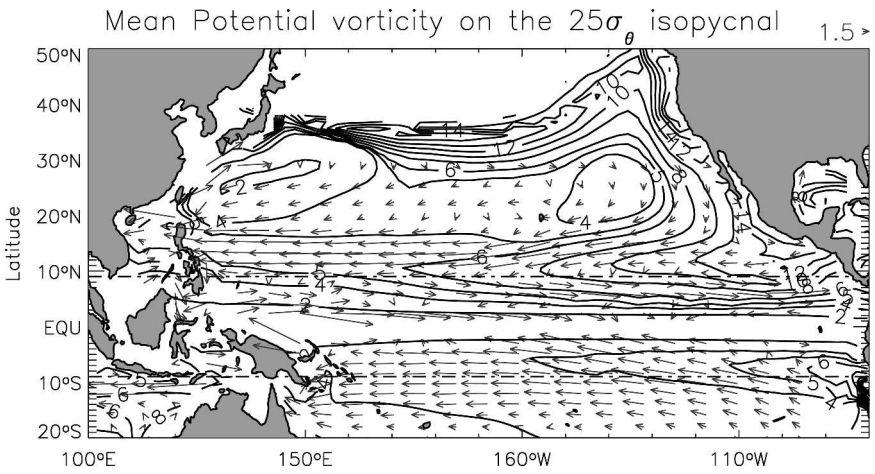

FIG. 2. Contours of mean potential vorticity over the 25 σ_θ isopycnal. The arrows indicate the averaged upper-ocean velocities, integrated from the base of the surface Ekman layer (~50-m depth) to the depth of the 25 σ_θ isopycnal.

nents of the meridional transports along 9°S and 9°N. The latitude of 9°N was chosen because it represents a choke point for the meridional geostrophic transport (Fig. 2), and 9°S was chosen for hemispheric symmetry. Sections of mean meridional velocities along 9°N and 9°S are shown in Fig. 3. Along both latitudes, the poleward Ekman transport is confined approximately to the upper 50 m, and the interior equatorward flow is found primarily above the mean 26 σ_θ isopycnal (thick solid lines in Figs. 3a and 3b), which is near the base of the pycnocline as defined in MPZ. Notice that at 9°N the largest equatorward interior flow occurs between approximately 180° and 140°W. East of 140°W, the communication between the Tropics and extratropics is impeded by the potential vorticity barrier, while west of the date line, the flow tends to be more zonal and will primarily feed the Mindanao current. At 9°S the largest interior flow extends from ~160° to ~90°W. Because of the absence of a potential vorticity barrier in the Southern Hemisphere, an intense equatorward flow can be found almost all the way to the eastern boundary. West of 160°W, currents are primarily westward and feed the New Guinea Coastal Current.

The zonally averaged interior transport is estimated by vertically integrating the meridional velocity from 50 m (the approximate depth of the Ekman layer) to the depth of the 26 σ_θ isopycnal and then integrating zonally from the eastern edge of the western boundary currents (137°E at 9°N and 160°E at 9°S) to the eastern boundary. The western boundary current transport is estimated by integrating the meridional velocity from the surface to the depth of the 26 σ_θ isopycnal and then zonally from the western boundary to 160°E at 9°S and 137°E at 9°N. At 9°N the mean transport of the western boundary current is 15.8 Sv (1 Sv $\equiv 10^6$ m^3 s^{-1}), and the interior transport is 5.4 Sv, while at 9°S the boundary current and interior transports are 8 and 9.6 Sv, respectively.

The value of the mean boundary current transport at 9°N is close but slightly higher than observational esti-

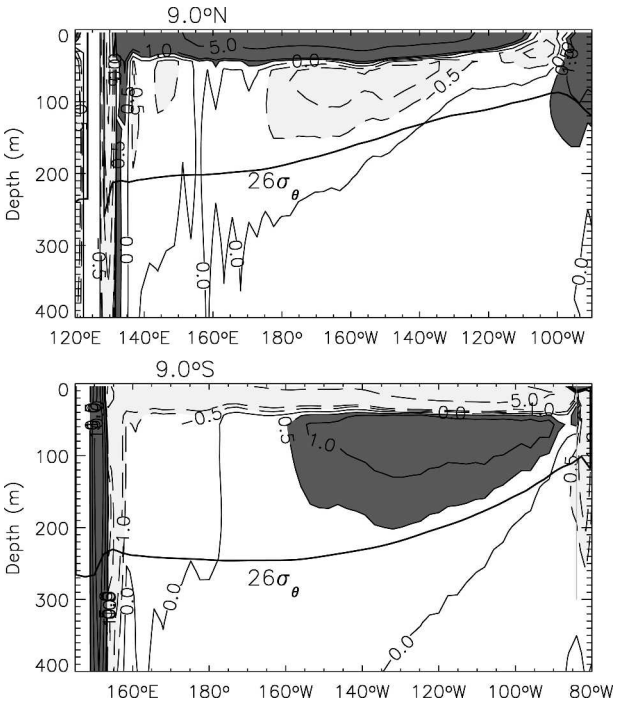

FIG. 3. Sections of mean meridional velocity at (top) 9°N and (bottom) 9°S. Dark shading indicates northward velocities, and light shading is for southward velocities. The poleward flow in the upper 50 m corresponds to the Ekman transport. The thick solid lines indicate the mean depth of the 26 σ_θ isopycnal.

mates: 13 Sv by Lukas et al. (1991) at 10°N based on Acoustic Doppler Current Profiler (ADCP) measurements, 15 Sv by Wijffels et al. (1995) at 8°N based on an inverse model of hydrography, and 14 Sv by Huang and Liu (1999) based on the NCEP ocean model. The model's interior transport at 9°N is very close to the 5-Sv value estimated by Johnson and McPhaden (1999) at 8°N using hydrographic data over the period 1967–98 and is a little higher than the value of 4 Sv obtained by Wijffels et al. (1995) and Huang and Liu (1999). The mean interior transport at 9°N from all hydrographic data over the period 1956–99 (MPZ) is ~7 Sv, higher than all other estimates. Thus, the model interior mean transport seems to be within the observational values.

The mean model transports in the western boundary current and interior at 9°S are smaller by a few Sverdrups than the available observational estimates (Lindstrom et al. 1987; Butt and Lindstrom 1994; Johnson and McPhaden 1999; Huang and Liu 1999). For reference, the mean interior transport from MPZ is 14 Sv. A similar discrepancy with observations was also found in the model examined by LF03. The model's underestimate of the western boundary current transport was primarily attributed to its inability to properly resolve the two branches of the western boundary current, the New Guinea and New Ireland Coastal Undercurrents, as identified by Lindstrom et al. (1987) and Butt and Lindstrom (1994), due to the limited model horizontal resolution. Similar limitations exist for the model used in the present study, whose horizontal resolution is also coarse. In addition, as noted by LF03, the mean wind forcing can have a large influence on the magnitude of the pycnocline transport, and it is plausible that the NCEP wind product underestimates the wind stress and wind stress curl in some regions.

The time series of the interior pycnocline transport anomalies at 9°N and 9°S are shown in Fig. 4a. The monthly anomalies have been obtained by subtracting the monthly means from the monthly averages of the OGCM output and then smoothing the resulting time series with a three-point binomial filter. In Fig. 4, the model's interior pycnocline transport anomalies are compared with the observational estimates of MPZ, computed for 1956–65, 1970–77, 1980–89, and 1990–99. Unfortunately, the period spanned by the model simulation (1958–97) does not exactly overlap with the period covered by the observational study (1950–99), so that it is not possible to compute averages from the model over the exact same periods. For the model, we compute averages for 1960–65, 1970–77, 1980–89, and 1990–97, which are compared in Fig. 4a with the observational values of MPZ. Notice that the period 1990–99 considered by MPZ includes the 1997–98 El Niño, of which the model only captures the initial phase. This may partially explain the model's underestimate of the transport decrease in the 1990s with respect to observations. Overall, however, the model transport anomalies are within the error bars of the observed values.

We then compute the meridional transport convergence in the interior pycnocline across 9°S and 9°N (Fig. 4b) and compare the values of transport convergence estimated by MPZ with the model averages over the same four periods used for the individual transports at 9°S and 9°N, as in Fig. 4a. The largest discrepancies are found in 1956–65, and in the 1990s, where the periods considered for the model do not fully overlap with the observational periods. However, the differences between model and observations tend to be within the observational error, and the decrease in transport from the early 1960s to the 1990s is ~11 Sv in both the model and observations. Thus, the model seems to provide a realistic representation of the transport changes, which makes it a suitable diagnostic tool to understand the processes underlying the transport variability.

In Fig. 5 the equatorward mass convergence in the interior pycnocline is compared with the changes in SST in the central and eastern equatorial Pacific (9°S–9°N, 90°W–180°), the same area considered by MPZ. Both time series are based on monthly anomalies and can be compared on all time scales, from interannual to decadal. Notice that SST is shown with the sign reversed for ease of comparison. Increased (decreased) mass convergence is associated with increased (decreased) upwelling and lower (higher) SSTs. As a result, the two time series are largely anticorrelated (correlation coefficient is −0.91), but the largest correlation is found when the SST leads the meridional mass convergence by 2 months, a result that seems to be in disagreement with the view that changes in the strength of the STCs cause the SST changes. The slight lag between interior mass convergence and SST variations relies primarily upon the zonally averaged perspective that we have adopted and that has also been adopted in most of the previous studies. When the three-dimensional evolution of the STCs is considered, the phase relationship between equatorward thermocline transport and equatorial SSTs emerges more clearly, as discussed in section 4.

b. The surface Ekman transport

The meridional Ekman transport per unit longitude can be computed from the surface zonal wind stress:

$$M_c = -\frac{\tau^x}{\rho_o f}, \tag{1}$$

where τ^x is the zonal component of the wind stress, f is

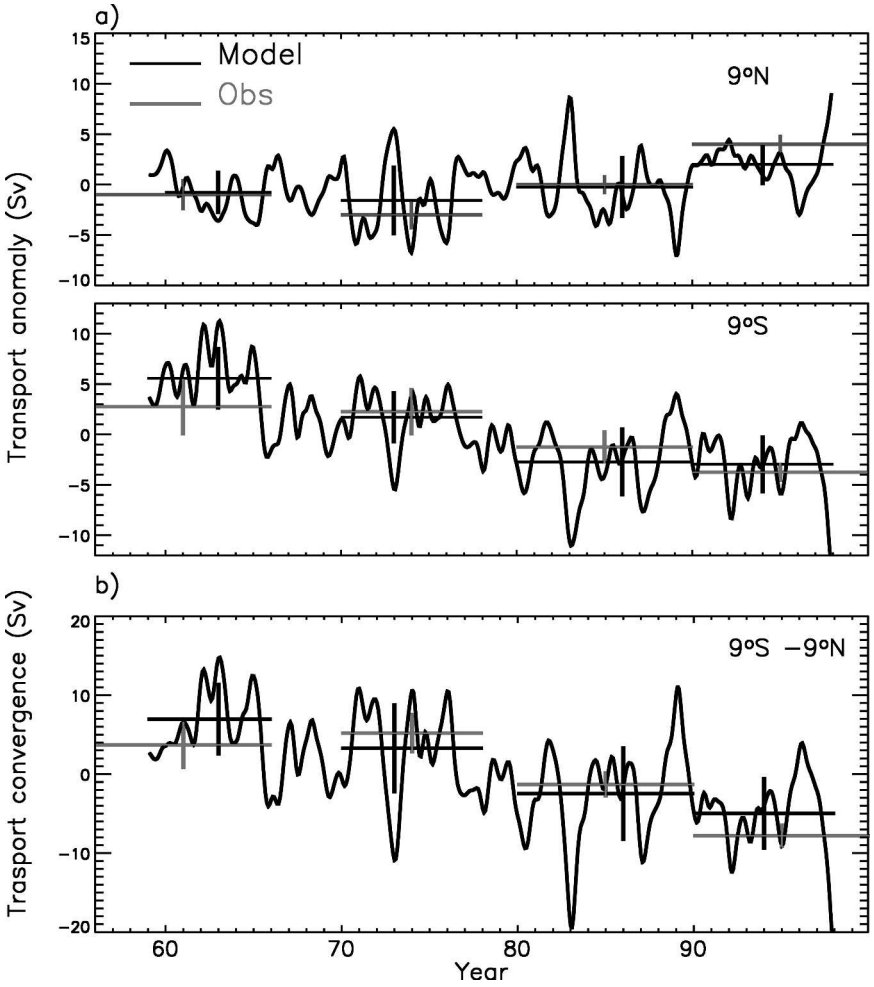

FIG. 4. (a) Interior pycnocline transport at (top) 9°N and (bottom) 9°S from the model. The time series are based on monthly anomalies and are smoothed using a 3-point binomial filter. The black horizontal lines are averages of the model pycnocline transports for 1960–65, 1970–77, 1980–89, and 1990–97. The black vertical lines show the standard deviations of the model monthly anomalies over each period. The gray horizontal lines are the observational estimates of MPZ for 1956–65, 1970–77, 1980–89, and 1990–99. The gray vertical lines indicate one standard error for the observational estimates. (b) Meridional transport convergence in the interior pycnocline across 9°S and 9°N. The horizontal black lines are the model averages for 1960–65, 1970–77, 1980–89, 1990–97, while the horizontal gray lines are the observational estimates of MPZ for 1956–65, 1970–77, 1980–89, and 1990–99. The error bars for the observational estimates are indicated by the vertical gray lines, while the vertical black lines show the standard deviations of the model monthly anomalies over each period.

the Coriolis parameter, and ρ_o is the mean density of seawater. The Ekman transport is to the right of the wind stress in the Northern Hemisphere and to the left of the wind stress in the Southern Hemisphere. Along 9°S and 9°N, τ^x is negative, so that the Ekman transports are poleward in both cases. Equation (1) has been integrated across the basin to obtain the zonally averaged Ekman transport. Figure 6 shows the comparison between the interior pycnocline transports at 9°S and 9°N and the surface Ekman transports along the same latitudes. The Ekman transports are shown with the sign reversed for ease of comparison. At 9°S the Ekman transport is highly correlated with the interior transport: the maximum correlation coefficient is −0.80 and occurs when EKM leads IN by 4 months. At 9°N the maximum correlation coefficient is −0.55 and is achieved when EKM leads IN by 9 months. The lags between EKM and IN along both latitudes are consistent with the view that the Ekman transport adjusts almost instantaneously to changes in the surface wind stress, while interior transport variations result from the ocean adjustment through Rossby wave propaga-

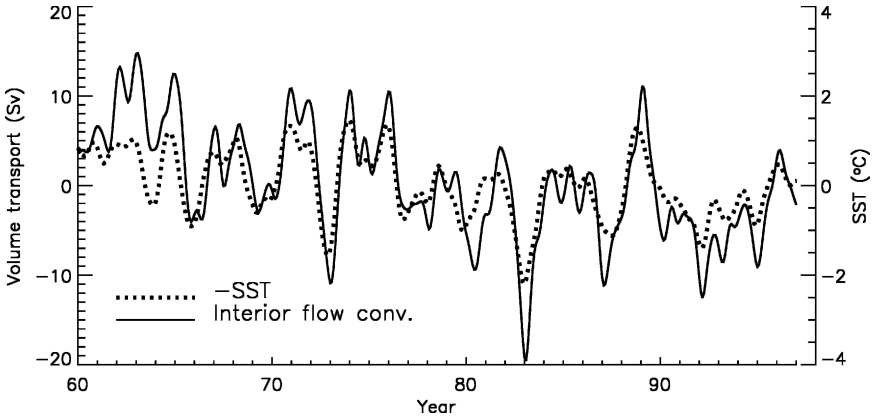

FIG. 5. Comparison between monthly anomalies of interior meridional mass transport convergence across 9°S and 9°N (solid line), and areally averaged SST variations over the central and eastern equatorial Pacific (9°S–9°N, 90°W–180°; dotted line). SST is plotted with the sign reversed for ease of comparison. The correlation between the two time series is −0.91, and it is achieved when the SST leads the transport convergence by 2 months. The correlation is significant at the 99% level, based on a *t*-test criterion with the number of degrees of freedom estimated according to Trenberth (1984).

tion, a much slower process. The large correlation between IN and EKM along 9°S and 9°N is an indication of the large influence of the local wind variations upon interior transport changes, in agreement with the results of Nonaka et al. (2002). The relationship between variations of STC strength and wind forcing will be further examined in section 5.

c. Interior versus boundary current transports

What is the relationship between equatorward pycnocline transports in the interior and in the western boundary currents? In Fig. 7 the interior transports are compared with the boundary current transports along 9°S and 9°N. The maximum correlation coefficients between the BC and IN time series are −0.76 (BC leads interior by 2 months) and −0.95 (lag 0 months) at 9°N and 9°S, respectively. The correlations around the maximum values decrease slowly as a function of lag, and the lag of 2 months between BC and IN at 9°N is statistically indistinguishable from 0. Thus, the transport changes in the boundary currents tend to compensate for the transport changes in the interior, especially at 9°S. The strong anticorrelation between boundary current changes and interior changes has been noted by other authors (Springer et al. 1990; LF03; Hazeleger et al. 2004; Wang et al. 2003a) in both realistic and idealized model simulations. LF03 have introduced a standard-deviation-based criterion to quantify the degree of compensation between IN and BC:

$$C = \frac{\sigma_{\mathrm{IN}} - \sigma_N}{\sigma_{\mathrm{IN}}} \times 100, \qquad (2)$$

where σ_{IN} and σ_N are the standard deviations of the interior transport and the net (IN + BC) transports, respectively. For the time series in Figs. 7a and 7b, the degrees of compensation, as expressed by C, are 22% and 69%, respectively. These values are comparable with those estimated by LF03 at 10°N (31%) and 10°S (62%) over the period 1980–2000.

LF03 have interpreted the anticorrelation in terms of time-dependent Sverdrup balance, which results from the adjustment of the low-latitude gyre circulation to varying Ekman pumping. Because of the finite adjustment time, one might expect the magnitude of the boundary current changes to depend upon the frequency of the forcing. We have examined the relationship between IN and BC at decadal (periods longer than 8 yr) and interannual (periods shorter than 8 yr) time scales. Our results (not shown) do not indicate any appreciable difference in levels of compensation in the two time-scale ranges. On the contrary, at 9°N the level of compensation is larger at interannual than decadal time scales. The correlation and level of compensation between BC and IN at decadal time scales are much higher at 13°N than at 9°N (not shown). As described in more detail in section 5, the latitude of 13°N is characterized by a local maximum in Rossby wave activity (Capotondi et al. 2003), which results in large thermocline displacements and meridional transport variations.

The Mindanao Current is one of the largest sources of ITF. Is the increase in the Mindanao Current transport after the mid-1970s feeding the ITF, or is it mainly affecting the mass balance of the tropical Pacific? Be-

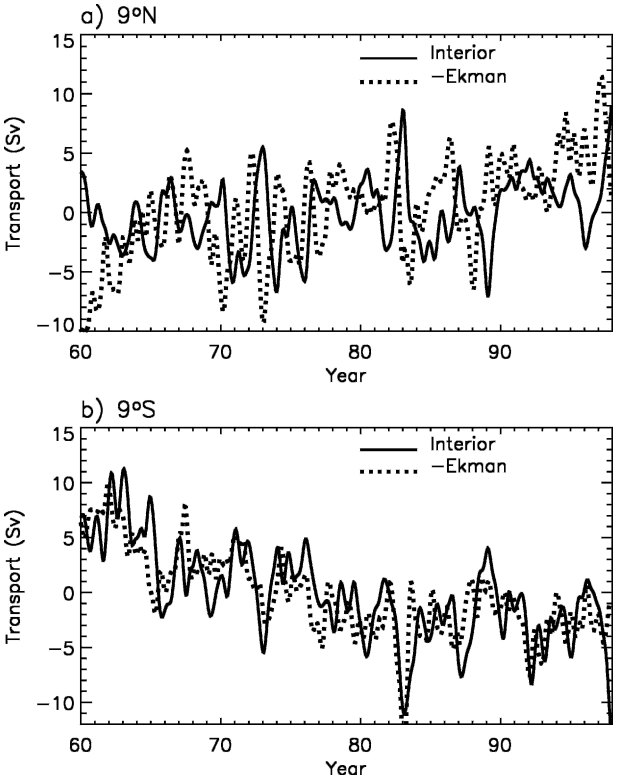

FIG. 6. Comparison between IN and EKM at (a) 9°N and (b) 9°S. All time series are based on monthly anomalies and are smoothed with a 3-point binomial filter. The Ekman transport time series is shown with the sign reversed for ease of comparison. At 9°N the maximum correlation coefficient between EKM and IN is −0.55 and is achieved when EKM leads IN by 9 months. At 9°S the max correlation coefficient is −0.80, with EKM leading IN by 4 months. The correlation between IN and EKM at 9°S is significant at the 99% level, while that at 9°N is only significant at the 95% level.

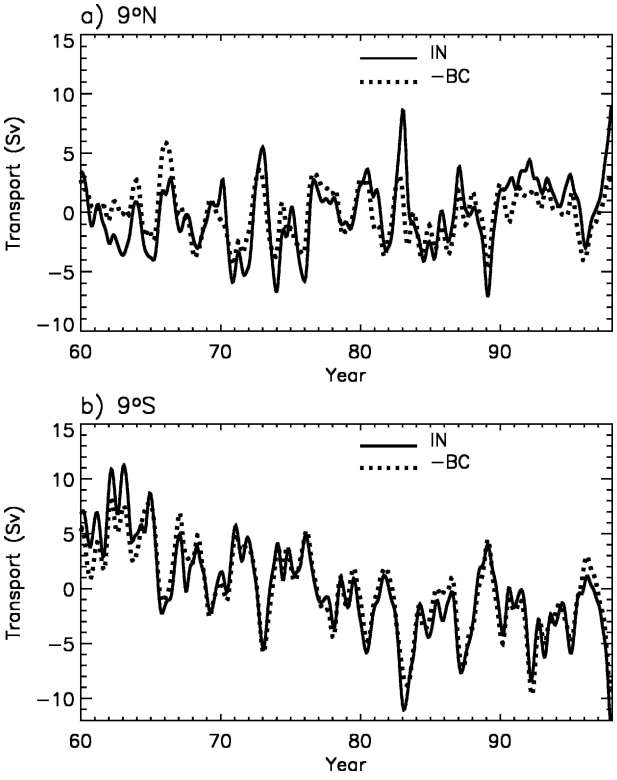

FIG. 7. Comparison between the evolution of the equatorward pycnocline transports in the interior and in the western boundary currents along (a) 9°N and (b) 9°S. All time series are based on monthly anomalies and are smoothed with a 3-point binomial filter. At 9°N the correlation coefficient is −0.76, with BC leading IN by 2 months. At 9°S the correlation coefficient is −0.95 at lag 0. At both latitudes, correlations are significant at the 99% level.

cause of the complex geometry of the Indonesian Archipelago, and the difficulty of tracking the pathways of the flow along the different passages, we examine the changes in ITF on the Indian Ocean side, along 115°E, from 20° to 9°S. The average ITF transport in the model, integrated from top to bottom, is 7.8 Sv. Observational estimates of total and partial ITF transports, using either direct or inverse methods, range from small negative values (flow from the Indian Ocean to the Pacific) to positive values close to 20 Sv (flow from the Pacific to the Indian Ocean; see Godfrey 1996 for a review). Using an inverse calculation, Macdonald (1998) estimates an ITF of 10 ± 10 Sv. Thus, the mean ITF transport in the model is within the range of observational estimates. The model ITF varies seasonally with a maximum in July–August of ~13.5 Sv and a minimum of ~4.5 Sv in January. Its seasonal variation is qualitatively consistent with that estimated by Meyers (1996) from expendable bathythermograph (XBT) data and those simulated by Masumoto and Yamagata (1996) and Lee et al. (2002).

The changes in the Indian Ocean outflow (integrated from the surface to the depth of the 26 σ_θ isopycnal and meridionally across the section) between 1977–97 and 1960–76 indicate a small decrease of the outflow (~0.3 Sv) after the mid-1970s, in spite of the increased transport of the Mindanao Current. Thus, variations in ITF cannot be expected to significantly alter the mass balance in the tropical Pacific. A similar conclusion was reached by LF03 for the changes during 1980–2000 and by MPZ for changes from the 1950s to the 1990s using the NCEP winds and Godfrey's Island Rule (Godfrey 1989).

d. Upwelling

The model mean vertical velocity (w) field is characterized by intense upwelling in a narrow band along the equator, extending from ~2°S to 2°N and from

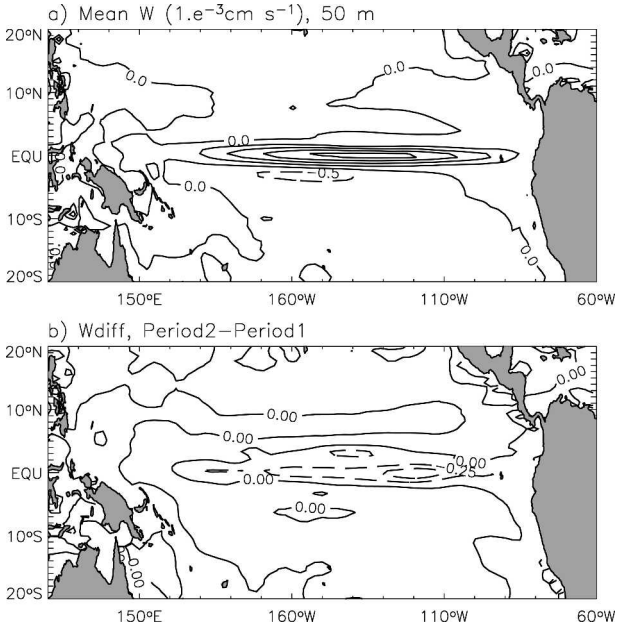

FIG. 8. (a) Mean vertical velocity over the period 1958–97 at 50-m depth. Contour interval is 0.5×10^{-3} cm s^{-1}. (b) Vertical velocity difference between Period2 (1977–97) and Period1 (1960–76) at 50-m depth. Contour interval is 0.25×10^{-3} cm s^{-1}.

175°E to 90°W (Fig. 8a), and continuing with lower values to the eastern boundary and along the coast of South America. The upwelling band along the equator is bounded on either side by broader and weaker downwelling areas, which are associated with the near-equatorial tropical cells. In the vertical plane, the largest upwelling occurs in the 40–90-m depth range (Fig. 1), close to the base of the Ekman layer, which is located at ~50-m depth.

To characterize the variability in the *w*-field, we start by considering the changes associated with the 1976–77 climate shift. Since the STCs appear to slow down after the mid-1970s, upwelling should also decrease after 1976. Figure 8b shows the differences in the *w*-field at 50 m between Period2 (1977–97) and Period1 (1962–75). The largest changes are found in the equatorial upwelling band, where the vertical velocity is ~20% weaker in Period2 versus Period1. This result is in disagreement with the findings of Klinger et al. (2002), based on idealized experiments forced by trade winds of different intensities. Klinger et al. (2002) showed that changes in the STC's strength are not associated with changes in the intensity of the equatorial upwelling, but with variations in the longitudinal extent of the upwelling region. On the contrary, in our OGCM simulation the longitudinal extent of upwelling remains approximately unchanged, while the amplitude of the upwelling exhibits a significant reduction. The idealized wind stress anomalies used by Klinger et al. (2002) did not include any anomalous forcing along the equator, a factor that may partially contribute to the differences with our results. The decreased upwelling along the equator and along the coast of South America in Fig. 8b is accompanied by a decreased downwelling on either side of the equator, indicative of a reduced strength of the tropical cells.

We can now consider the relationship between the upwelling strength and changes in SST over the region 9°S–9°N, 90°W–180°. Two different upwelling time series have been estimated: the first one (UPW1) is an average of the vertical velocity over the upwelling band (1°S–1°N, 90°W–180°), while the second time series (UPW2) is computed by averaging *w* over the same region used for SST (9°S–9°N, 90°W–180°). Thus, the first time series only captures the evolution of the upwelling, while the second time series averages out recirculations associated with the near equatorial tropical cells. The comparison between the SST evolution and the evolution of UPW1 is shown in Fig. 9. UPW1 has a correlation of 0.92 with SST and leads the SST by 1 month. When UPW2 is considered, the correlation drops to 0.78 with upwelling leading SST by 4 months (not shown), thus suggesting that the SST in the 9°S–9°N latitude band is primarily affected by upwelling variations in the very narrow equatorial band rather than by the average *w* changes in the 9°S–9°N region.

4. Three-dimensional evolution of the STCs

Several studies have examined the adjustment of the ocean circulation to changing wind forcing (Anderson and Gill 1975; Wang et al. 2003a; among others). In their seminal study, Anderson and Gill (1975) considered the spinup of a stratified ocean to the sudden onset of zonal wind stress, which was uniform in longitude and varied sinusoidally in latitude. The initial phase of the spinup away from the ocean boundaries consists of a local response to the Ekman pumping: as a consequence of the mass divergence (convergence) in the surface Ekman layer, the thermocline rises (deepens) linearly in time. The condition of non-normal flow through the eastern boundary is communicated to the interior by free planetary waves. Barotropic Rossby waves are faster than baroclinic Rossby waves and can cross the basin on a time scale of a few days. Thus, the barotropic adjustment is relatively fast. After the wave front has reached a given longitude, the steady Sverdrup balance is established at that longitude. The baroclinic adjustment is achieved through baroclinic Rossby wave propagation, and it occurs on longer time scales, as a result of the slower phase speed of the baroclinic

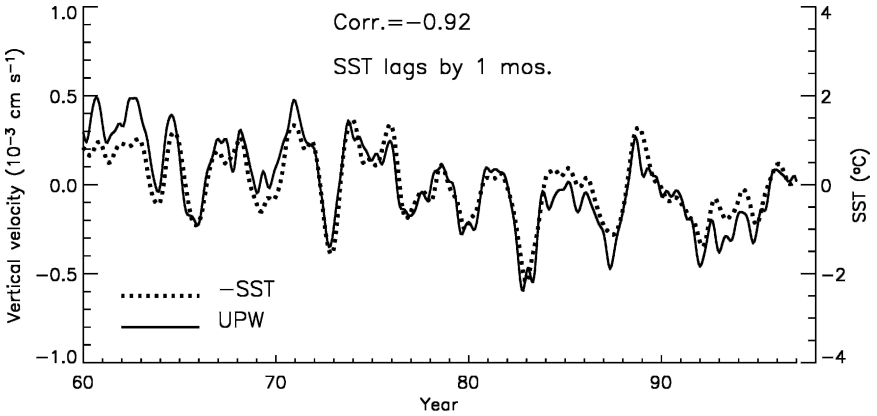

FIG. 9. Comparison of upwelling time series (areally averaged vertical velocity in 1°S–1°N, 90°W–180°; solid line; left axis) and SST anomaly time series (areally averaged SST over 9°S–9°N, 90°W–180°; dotted line; right axis). The SST anomaly time series is shown with the sign reversed to facilitate the comparison. Correlation coefficient between the two time series is −0.92, with UPW leading SST by 1 month. The correlation is significant at the 99% level. A vertical velocity of 1×10^{-3} cm s^{-1} corresponds to an upwelling transport of 22.5 Sv over the region 1°S–1°N, 90°W–180°.

modes. The western boundary current is the last component of the circulation to undergo the baroclinic adjustment and reach the final steady state.

The adjustment time scales are largely dependent upon the structure of the wind forcing. If, for example, the wind stress differs from zero only over limited latitude and longitude ranges, the adjustment time will depend upon the distance of the anomalous wind stress patch from the western boundary, and upon the average latitude of the patch, since the Rossby wave phase speed decreases with latitude. The dependence of the adjustment time upon the latitude and longitude of the anomalous wind forcing has been described by Wang et al. (2003a) based upon numerical experiments forced by idealized wind anomalies that were different from zero only over a small region.

In section 3 we have seen that the changes in the boundary current are simultaneous with the changes in the interior transport at 9°S and slightly ahead of the changes in the interior transport at 9°N. Also, the changes in the interior transport slightly lag the SST variations. Are the phase relationships between the different branches of the STCs consistent with the nature of the adjustment process? In our model simulation, the mean vertically integrated circulation (Fig. 10a) includes two tropical gyres characterized by anticlockwise flow in the Northern Hemisphere (negative values of the barotropic streamfunction) and clockwise flow in the Southern Hemisphere (positive streamfunction values). In Period2 the two gyres strengthen, leading to stronger boundary currents (Fig. 10b), so that the changes in the low-latitude western boundary currents appear to be associated with the adjustment of the horizontal gyres. If we examine the velocity difference in the zonal-vertical plane (Fig. 11), we notice that the largest velocity anomalies are found in the upper ocean, primarily above the 26 σ_θ isopycnal, indicating that the

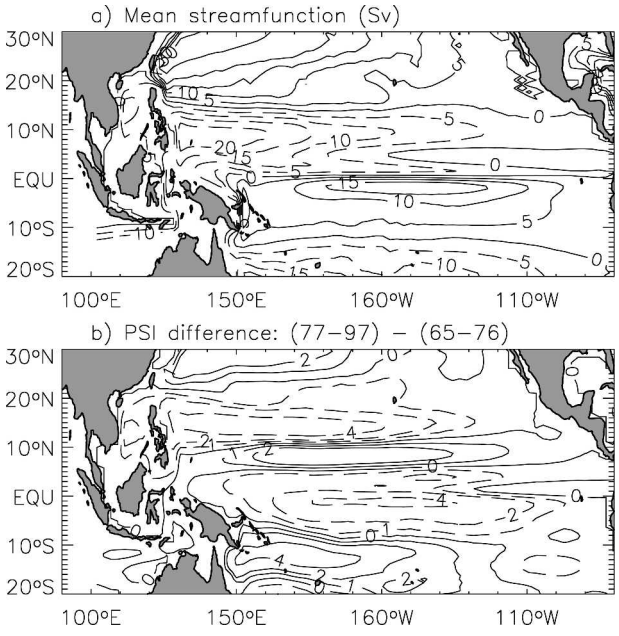

FIG. 10. (a) Time-averaged barotropic streamfunction. Solid contours are for positive values, and dashed contours are for negative values. Contour interval is 5 Sv. (b) Barotropic streamfunction differences between Period2 (1977–97) and Period1 (1965–76). Solid contours are for positive values, and dashed contours are for negative values. Contour interval is 2 Sv.

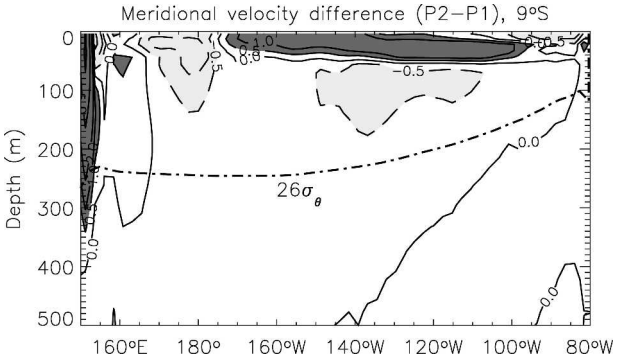

FIG. 11. Difference of meridional velocity section between Period2 (1977–97) and Period1 (1960–76), along 9°S. Contour interval is 0.5 cm s^{-1}. Positive differences are dark shaded, while negative differences are light shaded. The dotted–dashed line indicates the mean depth of the 26 σ_θ isopycnal. Notice the positive changes in the surface Ekman transport and the negative changes in the interior geostrophic transport, as well as the positive changes in the upper-western boundary current.

boundary current changes are of baroclinic nature and must result from first-mode baroclinic Rossby wave propagation. Thus, to examine the adjustment of the STCs under changing wind forcing, we seek evidence of baroclinic Rossby waves.

Figures 12a and 13a show the evolution of the depth of the 25.5 σ_θ isopycnal, a density surface that lies in the core of the main thermocline, along 13°N and 13°S, respectively. The latitude of 13°N has been chosen instead of 9°N because the transport changes are larger, and the relationship between interior and boundary transports is clearer. We chose 13°S for equatorial symmetry. Results are very similar at 9°N and 9°S, although propagation can be more easily visualized along 13°N and 13°S because of the slower phase speed. Figures 12a and 13a show that the pycnocline depth anomalies have a large zonal scale and extend from the western boundary to ~110°W, which is west of the eastern boundary. As shown by Capotondi and Alexander (2001), the signals west of 110°W along 9°N can be reproduced using a simple Rossby wave model forced by the same Ekman pumping field used to force the OGCM. The pycnocline depth disturbances close to the eastern boundary, for example, the weak negative signals in 1964 and 1971 and the positive signals in 1983, 1987, and 1992–93, are likely associated with boundary waves generated at the equator. These eastern boundary disturbances do not seem to propagate very far into the interior, a result consistent with the observational study of Kessler (1990).

If we view the ocean as a shallow-water system with a moving upper layer and a motionless bottom layer, the anomalous meridional upper-layer velocity v' is related to the zonal gradients of the upper-layer depth anomaly h':

$$v' = \frac{g'}{f}\frac{\partial h'}{\partial x}, \tag{3}$$

where g' is the reduced gravity, and f is the Coriolis parameter. The reduced gravity can be related to the local Rossby radius of deformation λ:

$$g' = \frac{\lambda^2 f^2}{H_0}, \tag{4}$$

where H_0 is the average upper-layer depth, so that the upper-layer anomalous transport V' can be expressed as

$$V' = f\lambda^2\frac{\partial h'}{\partial x}. \tag{5}$$

The anomalous transports from Eq. (5) along 13°N and 13°S are shown in Figs. 12b and 13b, respectively, and can be compared with the anomalous transports estimated from the OGCM by integrating the anomalous meridional velocity from the base of the Ekman layer to the depth of the 26σ_θ isopycnal along the same latitudes (Figs. 12c and 13c). The longitudinal distribution and time evolution of the transport anomalies in Figs. 12c and 13c are remarkably similar to those in Figs. 12b and 13b, clearly illustrating how the changes in transport at each longitude are associated with the passage of the baroclinic waves. It is also clear from Figs. 12b, 12c, 13b, and 13c that the changes in the boundary current result from the anomalous zonal gradients of thermocline depth, and the anticorrelation between interior transport changes and boundary current changes can be visualized as a consequence of the opposite sign of h'_x at the eastern and western sides of the thermocline depth anomaly. At 13°N the boundary current anomalies computed from the zonal gradient of h' (Fig. 12b) are weaker than those seen in Fig. 12c. The Mindanao Current originates from the bifurcation of the North Equatorial Current at the Philippines coast just to the north of 13°N. Thus, the width of the boundary current is relatively small at this latitude, and the transport changes can be easily underestimated using Eq. (5), by taking a zonal derivative in a coarse-resolution model. The boundary current changes from Eq. (5) are much more similar to those diagnosed from the OGCM at 13°S (see Figs. 13b and 13c). The large zonal scale of the thermocline depth anomalies, which in most cases extend almost all the way to the western boundary (Figs. 12a and 13a), seems to be the primary reason for the small temporal lag between variations in boundary current and interior transports described in section 3c.

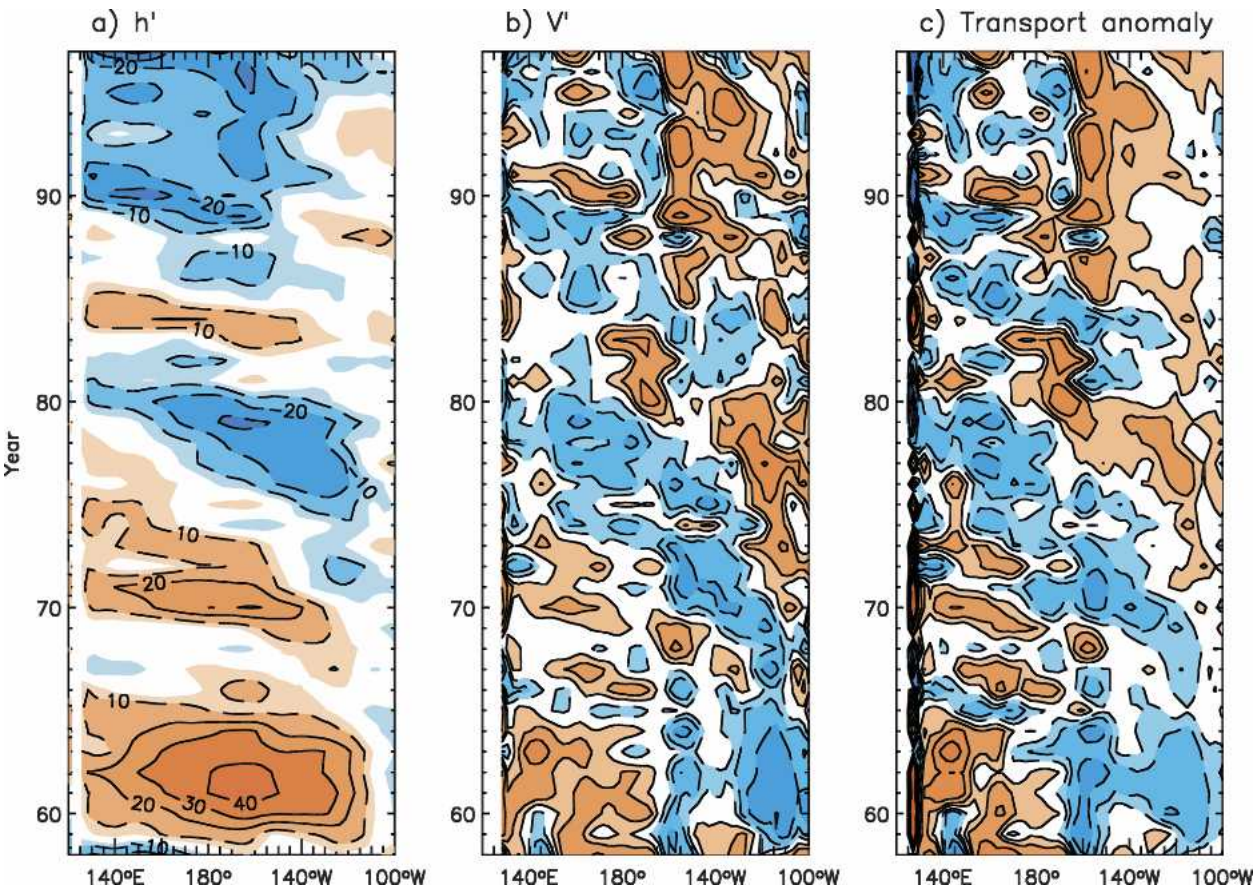

FIG. 12. (a) Evolution of the depth of the 25.5 σ_θ isopycnal along 13.6°N, as a function of longitude and time, based on annual mean values. Orange shading is for positive values (deeper thermocline), while the blue shading is for negative values (shallower thermocline). (b) Upper-ocean meridional transport anomalies based on Eq. (5), relating the transport anomalies to the zonal gradients of the thermocline depth. (c) Upper-ocean transport anomalies computed from the OGCM by integrating the meridional velocity vertically from the base of the Ekman layer to the depth of the 26 σ_θ isopycnal.

As seen from the slope of the phase lines in Figs. 12b, 12c, 13b, and 13c, the transport anomalies also exhibit westward propagation: changes in transport are not simultaneous along 13°N and 13°S, and they have different signs at different longitudes. For example, transport anomalies in 1978 are positive east of ~160°W at 13°N and negative west of that longitude (Fig. 12c). Thus, the zonal average of the interior transport anomalies can easily distort the phase relationship between variations in interior transport and other quantities. Figure 14 shows the lag-correlation between SST in the tropical box (9°S–9°N, 180°–90°W) and the interior mass convergence zonally averaged east of different longitudes. The lag-correlations are displayed in Fig. 14 as a function of temporal lag and the longitude defining the western edge of the range where the interior mass convergence is computed. Correlations remain statistically significant all the way across the basin, indicating that transport changes in the eastern part of the basin along 9°S and 9°N are relevant for SST changes, and the lag corresponding to the maximum correlation varies from negative values (SST leads interior mass convergence) when the interior transports are zonally averaged across the basin, to small positive values (interior mass convergence leads SST) when only the transports in the eastern part of the basin are considered. Thus, phase relationships among the different STC components can be largely affected by the zonal averaging procedure because of the continually evolving nature of the STCs. The lag between equatorial SST variations and zonally averaged interior transport convergence may also be due to the neglect of the heat transport by the zonal eddy component, where "eddy" refers to deviations from the zonal average. The zonally averaged meridional heat transport due to changes in the strength of the STCs can be written as

$$[v'\overline{T}] = [v'][\overline{T}] + [v'^*\overline{T}^*], \tag{6}$$

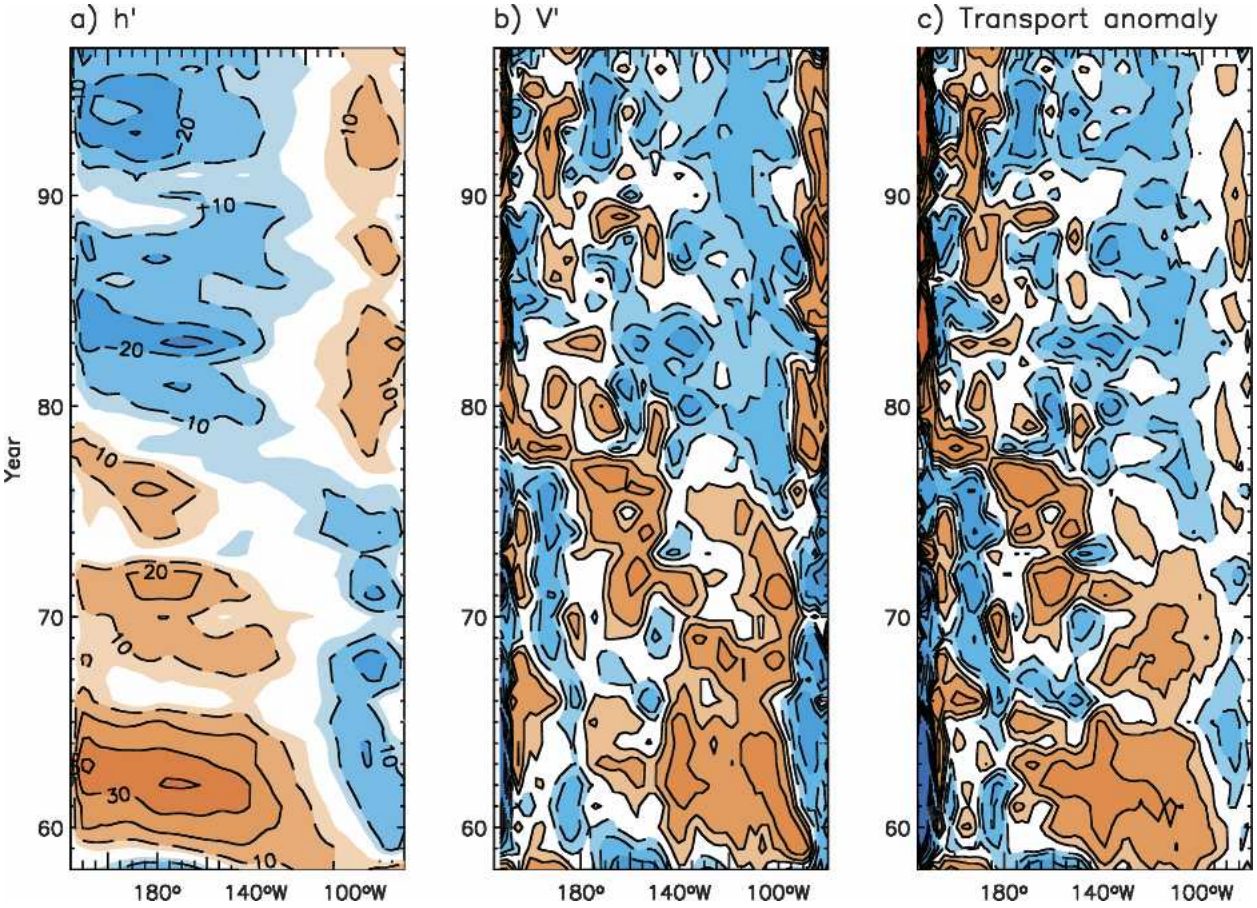

FIG. 13. Same as in Fig. 12, but for 13.6°S.

where v' is the anomalous (in time) meridional thermocline transport for unit longitude, $\overline{T}$ is the time average heat content for unit longitude, the square brackets indicate the zonal average, and the asterisks indicate the deviation from the zonal average. The equatorward mass convergence shown in Fig. 4 only accounts for the first term on the right-hand side (rhs) of Eq. (6). The second term, the eddy term, may also be significant (Hazeleger et al. 2004) and may alter the phase relationship between the equatorward heat transport and the equatorial SST. However, when the zonal average is computed east of the western boundary, as described in section 3a, the eddy term in Eq. (6) is about an order of magnitude smaller than the first term on the rhs. Also, the two terms are exactly opposite in phase, so that we cannot expect the eddy component of the heat transport to change the phase relationship between zonally averaged transport and SST. A detailed heat budget analysis is beyond the scope of the present study and will be examined in future work.

LF03 argued that variations in the boundary current and in the interior pycnocline transport may result from different forcing mechanisms: boundary current variations are part of the horizontal gyre adjustment and reflect the zonally integrated effect of the wind stress curl anomalies, particularly those in the western part of the basin. Variations in the interior transport, on the other hand, were related by LF03 not only to wind stress curl changes in the extraequatorial Tropics, but also to changes in the near-equatorial wind stress. The influence of the near-equatorial wind stress on the transport at 10°N (S) is achieved through equatorial Kelvin waves, which continue poleward along the eastern boundary as coastal Kelvin waves, radiating westward-propagating baroclinic Rossby waves. Our analysis illustrates and clarifies how both boundary and interior transport changes result from the baroclinic adjustment process.

5. What is the latitudinal range of the decadal STC changes?

The STCs are shallow overturning cells that extend from the equator to the subtropics (Fig. 1). Do they

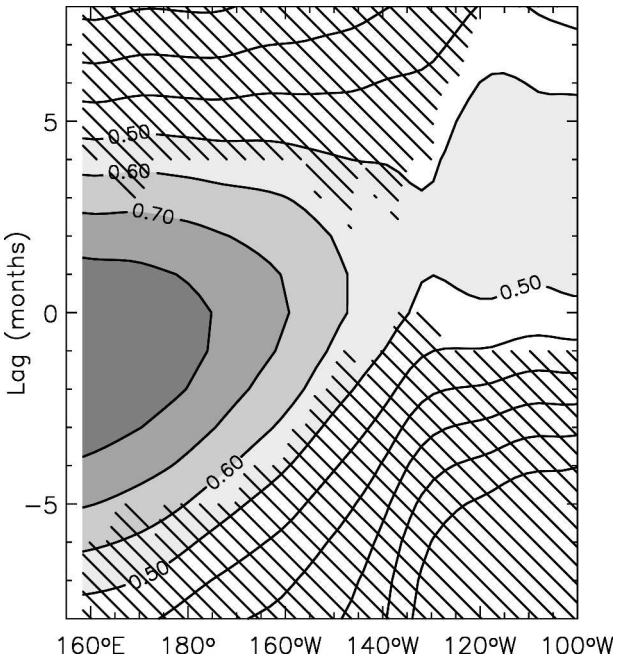

FIG. 14. Lag correlation between areally averaged SST over the region 9°S–9°N, 90°W–180° and equatorward mass convergence across 9°S–9°N in the interior pycnocline zonally averaged east of varying longitudes. The lag correlations are shown as a function of temporal lag and the western edge of the longitude range where the equatorward mass convergence is computed. Positive lags indicate that the equatorial mass convergence leads SST, and vice versa. The hatched areas indicate correlations that are not statistically significant at the 95% level. The statistical significance of correlations has been determined using a *t*-test criterion, with the number of degrees of freedom estimated according to Trenberth (1984).

spin up and spin down as a whole, or are the transport changes more pronounced in particular latitude ranges? As seen in section 4, changes in the meridional pycnocline transport are primarily associated with changes in the zonal slope of the thermocline. Thus, the spatial distribution of the pycnocline depth changes can give us an indication of the latitude range where transport variations are significant.

Differences in pycnocline depth between Period2 and Period1 (Fig. 15) show that the largest depth anomalies are generally confined to the 20°S–20°N latitude band. Within this band, the pycnocline is shallower in the west after the mid-1970s and slightly deeper in the east. Thus, the zonal slope of the tropical pycnocline is reduced after the mid-1970s, consistent with the decreased meridional transport. A similar pattern was computed from subsurface observations by MPZ as the difference between the pycnocline depth in 1990–99 versus 1970–77. Within the Tropics, the largest differences in pycnocline depth occur in the two bands centered around 10°S and 13°N. These latitudes correspond to the locations where the Ekman pumping is characterized by a large zonal coherency and can efficiently excite a vigorous Rossby wave field (Capotondi et al. 2003). The differences in zonally averaged interior pycnocline transports between Period2 and Period1 show a pronounced variation with latitude (Fig. 16, left). The largest changes in interior transports are found around 10°S and 13°N, the same locations of largest pycnocline depth changes. The variations in boundary current transport tend to compensate the changes in interior transport (Fig. 16, right), as described in section 3c. The largest changes are also found around 10°S and 13°N and are of opposite sign with respect to those in the interior. Thus, the pycnocline transport changes exhibit a strong latitudinal dependence, and the largest anomalies can be related to the local Ekman pumping (Capotondi et al. 2003).

Which wind stress anomalies are most influential in driving equatorial SST variations? Figure 17 shows the difference in wind stress between 1977–97 and 1960–76. Most of the changes in the zonal wind stress from Period1 to Period2 are confined to the 18°S–18°N latitude band, with the largest differences located near 7°S and 10°N and between ~160° and 110°W. The changes in zonal wind stress are associated with the weakening of the easterly trade winds in Period2 versus Period1, as shown by the wind stress differences in Fig. 17, so that the largest variations are found close to the latitudes where the trade winds achieve their maximum amplitudes. The weakening of the trade winds and associated strengthening of the midlatitude westerlies are a manifestation of the Pacific decadal oscillation (PDO; Mantua et al. 1997; Zhang et al. 1997).

To better understand the relationship between zonal wind stress and equatorial SST variations, we consider the lag correlation between the upwelling index UPW1 (defined in section 3d) and the zonal wind stress. The upwelling index is representative of subsurface processes that directly influence equatorial SSTs, and the zonal wind stress controls the meridional component of the Ekman transport, which is the surface branch of the STCs. To identify differences in the patterns of anomalous wind stress responsible for interannual and decadal variations the lag-correlation analysis has been computed for the two frequency bands separately. Decadal time scales have been isolated by low-pass filtering the data using a Fourier filter with half-power at 7.5 yr, while interannual time scales have been obtained by bandpass filtering the data with half-power at 1.5 and 7.5 yr. The results are shown in Fig. 18. At interannual time scales (Fig. 18a), the wind stress anomalies char-

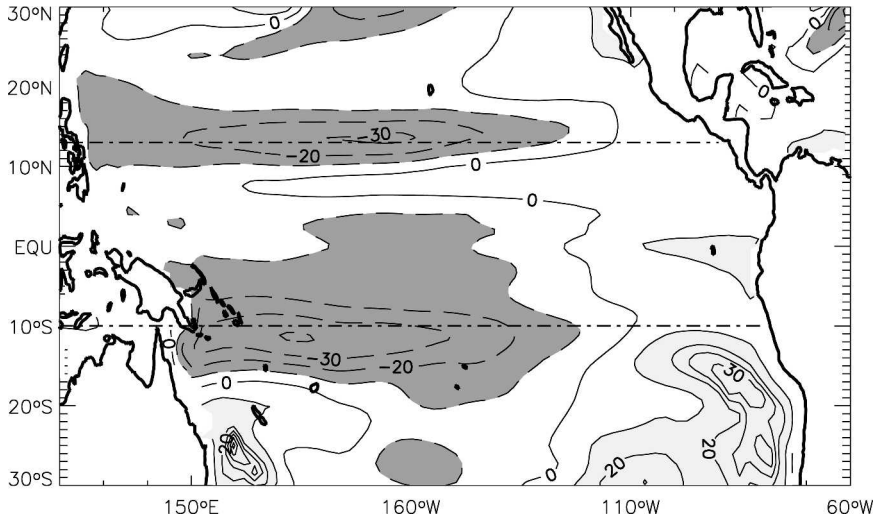

FIG. 15. Differences in pycnocline depth (described by the depth of the 25.5 σ_θ isopycnal) between 1977–97 and 1960–76. Dark shading is for negative differences (shallower pycnocline in Period2) whose absolute value is larger than 10 m, and light shading is for positive differences (deeper pycnocline in Period2) larger than 10 m. Contour interval is 10 m. The dotted–dashed lines indicate the latitudes of 10°S and 13°N.

acterized by the highest correlations with UPW1 are located in the central and western equatorial Pacific, with maximum values centered on the equator at ~160°W. Maximum correlations are negative, indicating that positive upwelling anomalies are associated with anomalous equatorial easterlies. At decadal time scales (Fig. 18b), the correlation pattern has a broader meridional scale, and the maximum correlations (>0.9)

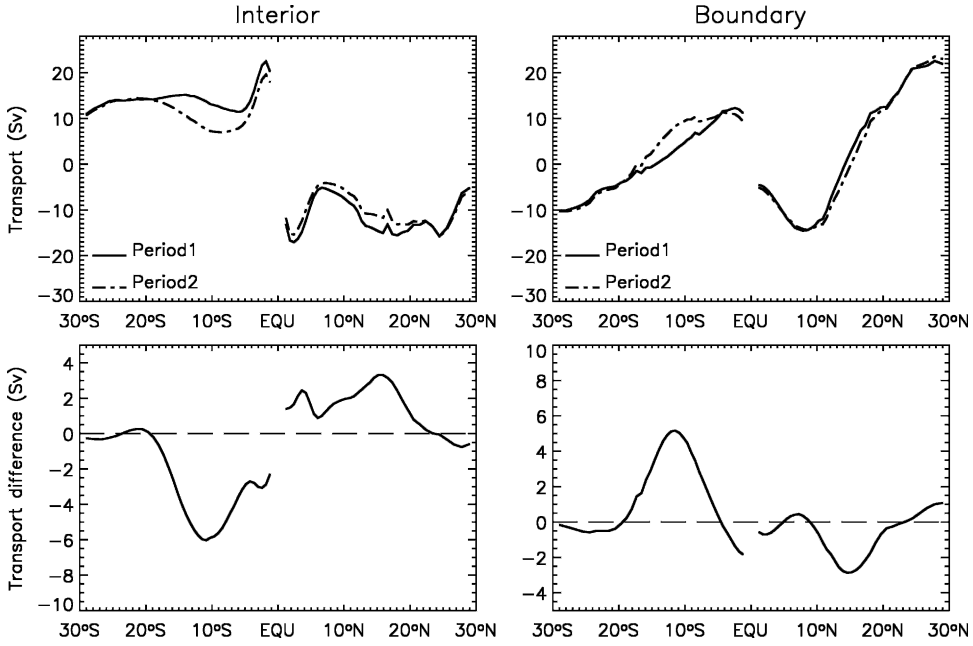

FIG. 16. (top left) The interior and (top right) boundary transports as a function of latitude for Period1 (1960–76; solid line) and Period2 (1977–97; dotted–dashed line). The differences (Period2 − Period1) of (bottom left) interior and (bottom right) boundary transports. Notice that the largest changes in both interior and boundary transports occur around 10°S and 13°N. The BC and IN transport changes are of opposite sign.

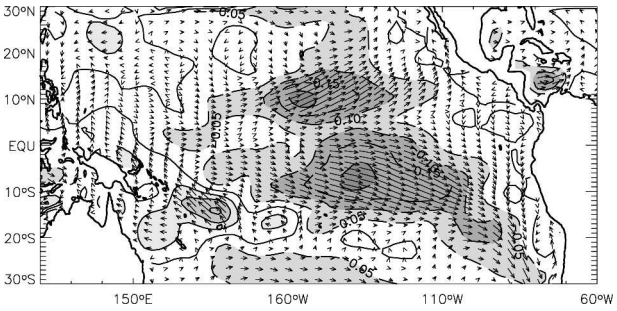

FIG. 17. Differences in zonal wind stress between 1977–97 and 1960–76 (contours). Contour interval is 0.05 dyn cm^{-2}. Solid contours are for positive values, while dashed contours are for negative values. Light shading is for zonal wind stress differences larger (in absolute value) than 0.05 dyn cm^{-2}, intermediate shading is for differences in the 1–2 dyn cm^{-2} range, and darker shading is for differences larger than 2 dyn cm^{-2}. Arrows show the difference in the total stress between the same two periods, indicating a weakening of the easterly trade winds.

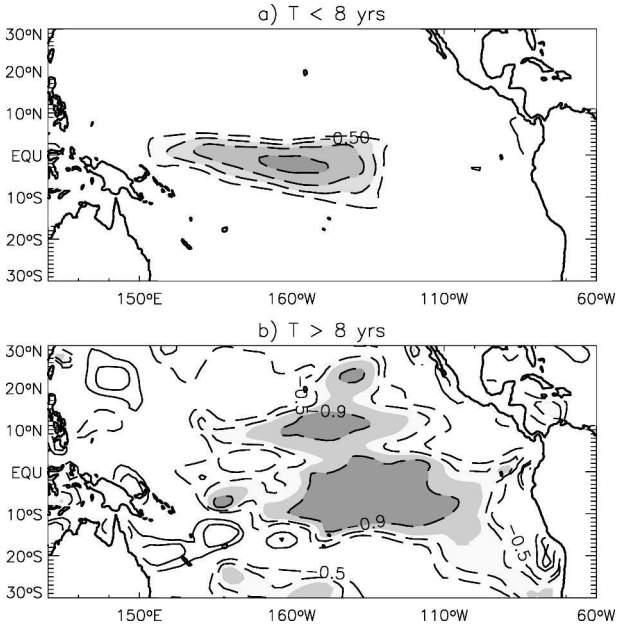

FIG. 18. (a) Max lag correlation between bandpass-filtered zonal wind stress and bandpass-filtered upwelling index (average of the vertical velocity at 50-m depth over the area 1°S–1°N, 90°W–180°), and (b) low-pass-filtered zonal wind stress and upwelling index. The filtering has been performed using a Fourier filter with half-power at 1.5 and 7.5 yr for the bandpass filter and 7.5 yr for the low-pass filter. Dashed contours are for negative values, and solid contours are for positive values. Negative correlations indicate that negative wind stress anomalies are associated with increased upwelling, and vice versa. In (a) the contour interval is 0.1, and only contours between −0.4 and 0.4 are shown. Correlations larger than 0.4 (in absolute value) are shaded. In (b) the contour interval is 0.2, and only values larger in absolute value than 0.5 are shown. Correlations whose absolute value is larger than 0.7 are shaded: light shading is for values between −0.7 and −0.8, intermediate shading is for values between −0.8 and −0.9, and darker shading is for absolute values larger than 0.9.

are found to the north and south of the equator, close to the areas of the largest low-frequency zonal wind stress variations seen in Fig. 17. The maximum correlations are negative: anomalous westerlies (weaker trade winds; positive anomalies) in the regions 12°S–equator, 160°–110°W and 7°–15°N, 160°–130°W are associated with decreased equatorial upwelling (slower STCs), and vice versa. The similarity between the correlation pattern in Fig. 18b and the zonal wind stress differences in Fig. 17 suggests that the largest correlations between UPW1 and τ^x in Fig. 18b are primarily associated with the 1976–77 climate shift. However, a similar correlation pattern is found also for the detrended low-pass-filtered anomalies, which only include decadal variations (not shown).

The correlation pattern at decadal time scales emphasizes the importance of wind variations within the 20°S–20°N latitude band for the low-frequency changes of equatorial SSTs. This result is consistent with the findings of Nonaka et al. (2002), who showed that wind variations outside the 25°S–20°N latitude band were unimportant for equatorial SST variability; Fig. 18 allows us to more specifically identify relevant forcing areas within the 20°S–20°N band. The correlation patterns in Fig. 18 support the theoretical study of Wang et al. (2003b), who showed that positive equatorial SST anomalies coupled to cyclonic wind stress anomalies in the eastern extraequatorial Tropics could produce oscillations with periods in the 10–15-yr range. Wang et al. (2003b) also showed that an ENSO-type oscillation (3–5 yr) could be generated from the coupling of positive SST anomalies and westerly wind stress in the central equatorial Pacific.

6. Conclusions

In this study we have used the output from an ocean general circulation model (OGCM) forced with observed surface fields to examine the evolution of the different branches of the Pacific subtropical–tropical cells and their impact on equatorial SSTs. Using subsurface observations over the period 1950–99, McPhaden and Zhang (2002) have shown that the equatorward pycnocline transports in the ocean interior along 9°S and 9°N have exhibited a decreasing trend since the 1970s, concurrent with a rise in equatorial SSTs. The transport variations in the model are similar to those estimated from observations, thus making the model a suitable diagnostic tool to better understand the STC evolution and its relationship with equatorial SST changes as well as changes in surface wind forcing.

Using the model output (available at a monthly resolution), we have been able to sharpen the observational perspective and have shown that the interior equatorward transports across 9°S and 9°N, as well as the mass convergence across those latitudes, are largely anticorrelated with equatorial SST changes at both interannual and decadal time scales. The interior pycnocline transports are also anticorrelated with the surface Ekman transports along the same latitudes, suggesting a strong connection with the local wind forcing. The poleward Ekman transport (the surface branch of the STC) leads by several months the changes in interior transport and SST, and the equatorial upwelling is strongly anticorrelated with SST changes and slightly leads them. However, when zonally averaged transports are considered, SST variations slightly lead (by ~2 months) the variations in interior transport, a result that seems in disagreement with the view that changes in the strength of the STCs cause changes in upwelling and equatorial SSTs. We should notice that correlations remain high over a broad range of lags, and small differences in correlations may not be statistically significant.

A better understanding of the relative timing of the different branches of the STCs can be gained by considering the three-dimensional evolution of the cells. Changes in equatorward pycnocline transport result from the baroclinic adjustment of the ocean circulation, which is accomplished through the westward propagation of baroclinic Rossby waves: anomalous Ekman pumping excites the baroclinic waves, which propagate westward and modify the ocean density structure, in particular the zonal gradient of thermocline depth, thus allowing anomalous meridional flows. Baroclinic Rossby wave propagation across the basin is a slow process (transit times can be of the order of a few years depending on the latitude), so that transport changes are not simultaneous at each longitude, but changes in the eastern part of the basin lead the changes in the western part. Variations in equatorial SSTs, spatially averaged over the central and eastern Pacific, result from an integrated effect of the equatorial mass convergence variations at each longitude, but the phase relationship between transport changes and SST changes can be distorted by zonally averaging the equatorward transports.

Using the model output, we have been able to examine the evolution of the transports in the low-latitude western boundary currents, which are poorly resolved by the observational record. Variations in boundary current transport are strongly anticorrelated with the changes in equatorward transport in the interior, indicating a tendency for the boundary current to compensate for the interior transport changes. The compensation is not complete, but the degree of compensation can be very large, as discussed by Lee and Fukumori (2003). They attributed the partial compensation to different forcing mechanisms for the interior and boundary current transports: while the boundary current variations are associated with the adjustment of the horizontal gyres to changes in Ekman pumping, the interior transport changes may also result from variations in near-equatorial surface wind stress with no curl. Our results highlight how changes in both interior and boundary currents are a consequence of the baroclinic adjustment of the ocean to large-scale wind stress curl variations, in agreement with the process study of Wang et al. (2003a).

The decadal evolution of the STCs appears to be forced by variations in the trade winds, whose largest changes are confined within 20° of the equator. The variations in pycnocline transport are also limited to the 20°S–20°N latitude band and exhibit a strong latitudinal dependence, with the largest changes located along those latitudes where the Ekman pumping can more efficiently excite baroclinic Rossby waves because of its large spatial coherency (Capotondi et al. 2003). Thus, transport variations of the various branches of the STCs can be largely related to local forcing within the Tropics, a somewhat different perspective from the one originally proposed by Kleeman et al. (1999), where changes in mass convergence/divergence in the subtropics were viewed as the driving mechanism of the STCs.

In summary, our results support the notion that variations in equatorward mass transport may drive SST variations in the central and eastern equatorial Pacific. However, some open questions remain. First, what are the consequences of the large degree of compensation between interior and boundary transport upon the equatorial heat balance? Second, what is the origin of the decadal wind stress variations in the tropical Pacific that initiate the STC variations? Are they a response to tropical SST anomalies, the tropical manifestation of midlatitude atmospheric circulation changes, or simply the low-frequency tail of internal atmospheric variability? Further studies using coupled simulations are needed to answer these questions.

Acknowledgments. We thank the NCAR Oceanography Section for making the model output available to us. Drs. Dongxiao Zhang, Tong Lee, and Zhengiu Liu and two anonymous reviewers have provided very useful insights for this study. AC and MJM acknowledge NOAA's Office of Oceanic and Atmospheric Research and Office of Global Program for support.

REFERENCES

Anderson, D. L. T., and A. E. Gill, 1975: Spin-up of a stratified ocean with application to upwelling. *Deep-Sea Res.,* **22,** 583–596.

Butt, J., and E. Lindstrom, 1994: Currents off the east coast of New Ireland, Papua New Guinea, and their relevance to regional undercurrents in the western equatorial Pacific Ocean. *J. Geophys. Res.,* **99,** 12 503–12 514.

Capotondi, A., and M. A. Alexander, 2001: Rossby waves in the tropical North Pacific and their role in decadal thermocline variability. *J. Phys. Oceanogr.,* **31,** 3496–3515.

——, ——, and C. Deser, 2003: Why are there Rossby wave maxima in the Pacific at 10°S and 13°N? *J. Phys. Oceanogr.,* **33,** 1549–1563.

Chang, P., B. S. Giese, H. F. Seidel, and F. Wang, 2001: Decadal change in the South Tropical Pacific in a global assimilation analysis. *Geophys. Res. Lett.,* **28,** 3461–3464.

Deser, C., M. A. Alexander, and M. S. Timlin, 1996: Upper-ocean thermal variations in the North Pacific during 1970–1991. *J. Climate,* **9,** 1840–1855.

——, A. S. Phillips, and J. W. Hurrel, 2004: Pacific interdecadal climate variability: Linkages between the Tropics and the North Pacific during boreal winter since 1900. *J. Climate,* **17,** 3109–3124.

Doney, S. C., S. Yeager, G. Danabasoglu, W. G. Large, and J. C. McWilliams, 2003: Modeling global oceanic interannual variability (1958–1997): Simulation design and model-data evaluation. NCAR Tech. Note NCAR/TN-452+STR, 48 pp.

Gent, P. R., and J. C. McWilliams, 1990: Isopycnal mixing in ocean circulation models. *J. Phys. Oceanogr.,* **20,** 150–155.

——, F. O. Bryan, G. Danabasoglu, S. C. Doney, W. R. Holland, W. G. Large, and J. C. McWilliams, 1998: The NCAR Climate System Model global ocean component. *J. Climate,* **11,** 1287–1306.

Godfrey, J. S., 1989: A Sverdrup model of the depth-integrated flow of the World Ocean allowing for island circulations. *Geophys. Astrophys. Fluid Dyn.,* **45,** 89–112.

——, 1996: The effect of the Indonesian throughflow on ocean circulation and heat exchange with the atmosphere: A review. *J. Geophys. Res.,* **101,** 12 217–12 237.

Gu, D., and S. G. H. Philander, 1997: Interdecadal climate fluctuations that depend on exchange between the Tropics and extratropics. *Science,* **275,** 805–807.

Haney, R. L., 1971: Surface thermal boundary condition for ocean circulation models. *J. Phys. Oceanogr.,* **1,** 241–248.

Hazeleger, W., R. Seager, M. A. Cane, and N. H. Naik, 2004: How can tropical Pacific Ocean heat transport vary? *J. Phys. Oceanogr.,* **34,** 320–333.

Huang, B., and Z. Liu, 1999: Pacific subtropical-tropical thermocline water exchange in the National Centers for Environmental Prediction ocean model. *J. Geophys. Res.,* **104,** 11 065–11 076.

Johnson, G. C., and M. J. McPhaden, 1999: Interior pycnocline flow from the subtropical to the equatorial Pacific Ocean. *J. Phys. Oceanogr.,* **29,** 3073–3089.

Kalnay, E., and Coauthors, 1996: The NCEP/NCAR 40-Year Reanalysis Project. *Bull. Amer. Meteor. Soc.,* **77,** 437–471.

Kessler, W. S., 1990: Observations of long Rossby waves in the northern tropical Pacific. *J. Geophys. Res.,* **95,** 5183–5217.

Kleeman, R., J. P. McCreary, and B. A. Klinger, 1999: A mechanism for generating ENSO decadal variability. *Geophys. Res. Lett.,* **26,** 1743–1746.

Klinger, B. A., J. P. McCreary, and R. Kleeman, 2002: The relationship between oscillating subtropical wind stress and equatorial temperature. *J. Phys. Oceanogr.,* **32,** 1507–1521.

Knudson, T. R., and S. Manabe, 1998: Model assessment of decadal variability and trends in the tropical Pacific Ocean. *J. Climate,* **11,** 2273–2296.

Large, W. G., and S. Pond, 1982: Sensible and latent heat flux measurements over the ocean. *J. Phys. Oceanogr.,* **12,** 464–482.

——, J. C. McWilliams, and S. C. Doney, 1994: Oceanic vertical mixing: A review and a model with a nonlocal boundary layer parameterization. *Rev. Geophys.,* **32,** 363–403.

——, G. Danabasoglu, and S. C. Doney, 1997: Sensitivity to surface forcing and boundary layer mixing in a global ocean model: Annual-mean climatology. *J. Phys. Oceanogr.,* **27,** 2418–2447.

——, J. C. McWilliams, P. R. Gent, and F. O. Bryan, 2001: Equatorial circulation of a global ocean climate model with anisotropic horizontal viscosity. *J. Phys. Oceanogr.,* **31,** 518–536.

Latif, M., and T. P. Barnett, 1996: Decadal climate variability over the North Pacific and North America: Dynamics and predictability. *J. Climate,* **9,** 2407–2423.

Lee, T., and I. Fukumori, 2003: Interannual-to-decadal variations of tropical–subtropical exchange in the Pacific Ocean: Boundary versus interior pycnocline transports. *J. Climate,* **16,** 4022–4042.

——, ——, D. Menemenlis, Z. Xing, and L.-L. Fu, 2002: Effects of the Indonesian Throughflow on the Pacific and Indian Oceans. *J. Phys. Oceanogr.,* **32,** 1404–1429.

Lindstrom, E., R. Lukas, R. Fine, E. Firing, S. Godfrey, G. Meyers, and M. Tsuchiya, 1987: The western equatorial Pacific Ocean circulation study. *Nature,* **330,** 533–537.

Liu, Z., 1994: A simple model of the mass exchange between the subtropical and tropical ocean. *J. Phys. Oceanogr.,* **24,** 1153–1165.

——, S. G. H. Philander, and R. C. Pakanowski, 1994: A GCM study of tropical–extratropical upper-ocean water exchange. *J. Phys. Oceanogr.,* **24,** 2606–2623.

Lukas, R., 1988: Interannual fluctuations of the Mindanao Current inferred from sea level. *J. Geophys. Res.,* **93,** 6744–6748.

——, E. Firing, P. Hacker, P. L. Richardson, C. A. Collins, R. Fine, and R. Gammon, 1991: Observations of the Mindanao Current during the Western Equatorial Pacific Ocean Circulation study. *J. Geophys. Res.,* **96,** 7089–7104.

Luo, J.-J., and T. Yamagata, 2001: Long-term El Niño-Southern Oscillation (ENSO)-like variation with special emphasis on the South Pacific. *J. Geophys. Res.,* **106,** 22 211–22 227.

Luyten, J. R., J. Pedlosky, and H. Stommel, 1983: The ventilated thermocline. *J. Phys. Oceanogr.,* **13,** 292–309.

Macdonald, A. M., 1998: The global ocean circulation: A hydrographic estimate and regional analysis. *Progress in Oceanography,* Vol. 41, Pergamon, 281–382.

Mantua, N. J., S. R. Hare, Y. Zhang, J. M. Wallace, and R. Francis, 1997: A Pacific interdecadal climate oscillation with impacts on salmon production. *Bull. Amer. Meteor. Soc.,* **78,** 1069–1079.

Masumoto, Y., and T. Yamagata, 1996: Seasonal variations of the Indonesian Throughflow in a general ocean circulation model. *J. Geophys. Res.,* **101,** 12 287–12 294.

McCreary, J. P., and P. Lu, 1994: Interaction between the subtropical and equatorial ocean circulations: The subtropical cell. *J. Phys. Oceanogr.,* **24,** 466–497.

McPhaden, M. J., and D. Zhang, 2002: Slowdown of the meridi-

onal overturning circulation in the upper Pacific Ocean. *Nature,* **415,** 603–608.

Meyers, G., 1996: Variation of Indonesian throughflow and the El Niño-Southern Oscillation. *J. Geophys. Res.,* **101,** 12 255–12 264.

Niiler, P., D.-K. Lee, and J. Moisan, 2004: Observed mechanisms of El Niño SST evolution in the Pacific. *J. Mar. Res.,* **62,** 771–786.

Nitta, T., and S. Yamada, 1989: Recent warming of tropical sea surface temperature and its relationship to the Northern Hemisphere Circulation. *J. Meteor. Soc. Japan,* **67,** 375–383.

Nonaka, M., S.-P. Xie, and J. P. McCreary, 2002: Decadal variations in the subtropical cells and equatorial Pacific SST. *Geophys. Res. Lett.,* **29,** 1116, doi:10.1029/2001GL013717.

Schneider, N., A. J. Miller, M. A. Alexander, and C. Deser, 1999: Subduction of decadal North Pacific temperature anomalies: Observations and dynamics. *J. Phys. Oceanogr.,* **29,** 1056–1070.

Solomon, A., J. P. McCreary Jr., R. Kleeman, and B. A. Klinger, 2003: Interannual and decadal variability in an intermediate coupled model of the Pacific region. *J. Climate,* **16,** 383–405.

Springer, S. R., M. J. McPhaden, and A. J. Busalacchi, 1990: Oceanic heat content variability in the tropical Pacific during the 1982–1983 El Niño. *J. Geophys. Res.,* **95,** 22 089–22 101.

Tanimoto, Y., N. Iwasaka, K. Hanawa, and Y. Toba, 1993: Characteristic variations of sea surface temperature with multiple time scales in the North Pacific. *J. Climate,* **6,** 1153–1160.

Timmermann, A., and F.-F. Jin, 2002: A nonlinear mechanism for decadal El Niño amplitude changes. *Geophys. Res. Lett.,* **29,** 1003, doi:10.12029/2001GL013369.

Trenberth, K. E., 1984: Some effects of finite sample size and persistence on meteorological statistics. Part I: Autocorrelations. *Mon. Wea. Rev.,* **112,** 2359–2368.

——, 1990: Recent observed interdecadal climate changes in the Northern Hemisphere. *Bull. Amer. Meteor. Soc.,* **71,** 988–993.

——, and J. W. Hurrell, 1994: Decadal atmosphere-ocean variations in the Pacific. *Climate Dyn.,* **9,** 303–319.

Wang, X., F.-F. Jin, and Y. Wang, 2003a: A tropical ocean recharge mechanism for climate variability. Part I: Equatorial heat content changes induced by the off-equatorial wind. *J. Climate,* **16,** 3585–3598.

——, ——, and ——, 2003b: A tropical ocean recharge mechanism for climate variability. Part II: A unified theory for decadal and ENSO modes. *J. Climate,* **16,** 3599–3616.

Wang, X. L., and C. F. Ropelewski, 1995: An assessment of ENSO-scale secular variability. *J. Climate,* **8,** 1584–1589.

Wijffels, S., E. Firing, and J. Toole, 1995: The mean structure and variability of the Mindanao Current at 8°N. *J. Geophys. Res.,* **100,** 18 421–18 435.

Yasuda, T., and K. Hanawa, 1997: Decadal changes in mode waters in the midlatitude North Pacific. *J. Phys. Oceanogr.,* **27,** 858–870.

Zhang, Y., J. M. Wallace, and D. S. Battisti, 1997: ENSO-like interdecadal variability: 1900–93. *J. Climate,* **10,** 1004–1020.